Charged pion production in $^{96}_{44}$Ru + $^{96}_{44}$Ru collisions at $400A$ and $1528A$ MeV

B. Hong,[1,*] Y.J. Kim,[1,2] N. Herrmann,[3] M.R. Stockmeier,[3] A. Andronic,[2] V. Barret,[4] Z. Basrak,[5] N. Bastid,[4] M.L. Benabderrahmane,[3] R. Čaplar,[5] P. Crochet,[4] P. Dupieux,[4] M. Dželalija,[5] Z. Fodor,[6] A. Gobbi,[2] Y. Grishkin,[7] O.N. Hartmann,[2] K.D. Hildenbrand,[2] J. Kecskemeti,[6] M. Kirejczyk,[8,2] P. Koczon,[2] M. Korolija,[5] R. Kotte,[9] T. Kress,[2] A. Lebedev,[7] Y. Leifels,[2] X. Lopez,[4] A. Mangiarotti,[3] M. Merschmeyer,[3] W. Neubert,[9] D. Pelte,[3] M. Petrovici,[10] F. Rami,[11] W. Reisdorf,[2] A. Schüttauf,[2] Z. Seres,[6] B. Sikora,[8] K.S. Sim,[1] V. Simion,[10] K. Siwek-Wilczyńska,[8] V. Smolyankin,[7] G. Stoicea,[10] Z. Tyminski,[8,2] P. Wagner,[11] K. Wiśniewski,[8] D. Wohlfarth,[9] Z.G. Xiao,[2] I. Yushmanov,[12] and A. Zhilin[7]

(FOPI Collaboration)

[1]*Korea University, Seoul, Korea*
[2]*Gesellschaft für Schwerionenforschung, Darmstadt, Germany*
[3]*Physikalisches Institut der Universität Heidelberg, Heidelberg, Germany*
[4]*Laboratoire de Physique Corpusculaire, IN2P3/CNRS, and Université Blaise Pascal, Clermont-Ferrand, France*
[5]*Ruđer Bošković Institute, Zagreb, Croatia*
[6]*KFKI Research Institute for Particle and Nuclear Physics, Budapest, Hungary*
[7]*Institute for Theoretical and Experimental Physics, Moscow, Russia*
[8]*Institute of Experimental Physics, Warsaw University, Warsaw, Poland*
[9]*IKH, Forschungszentrum Rossendorf, Dresden, Germany*
[10]*Institute for Nuclear Physics and Engineering, Bucharest, Romania*
[11]*Institut de Recherches Subatomiques and Université Louis Pasteur, Strasbourg, France*
[12]*Kurchatov Institute, Moscow, Russia*

We present transverse momentum and rapidity spectra of charged pions in central Ru + Ru collisions at $400A$ and $1528A$ MeV. The data exhibit enhanced production at low transverse momenta compared to the expectations from the thermal model that includes the decay of $\Delta(1232)$-resonances and thermal pions. Modification of the Δ-spectral function and the Coulomb interaction are necessary to describe the detailed shape of the transverse momentum spectra. Within the framework of the thermal model, the freeze-out radii of pions are similar at both beam energies. The IQMD model reproduces the shapes of the transverse momentum and rapidity spectra of pions, but the predicted absolute yields are larger than in the measurements, especially at lower beam energy.

PACS numbers: 25.75.Dw, 25.75.Ld

I. INTRODUCTION

Collision of relativistic heavy ions is a unique method to produce a large volume of excited nuclear matter in the laboratory at present. At incident beam energies near 1 GeV per nucleon nuclear matter can reach its density about two to three times higher than normal nuclear matter density at the temperature below 100 MeV [1, 2]. Major motivations for such studies aim to determine the nuclear equation of state (EoS) and to study the basic properties of quantum chromodynamics (QCD), the theory of strong interactions. These informations are important not only in their own virtue but also for understanding the behavior of astrophysical objects, such as neutron stars and supernovae [3].

Experiments of this kind started with various ion beams at the BEVALAC in 70's [4, 5]. Since the early 90's the heavy ion synchrotron SIS at GSI-Darmstadt, Germany, took over a leading role in relativistic heavy ion collisions in the energy range up to $2A$ GeV. A scenario of several complementary experimental setups at SIS has allowed to perform thorough investigations of the EoS and in-medium properties of hadrons [6, 7, 8, 9, 10].

Several observables, which are accessible in experiments, have been proposed as sensitive probes to characterize the properties of hot and dense nuclear matter. Among the prominent candidates are the collective flow [11, 12] and the particle production [13]. Especially the production of pions has been suggested rather early [14], as their yield can be connected to the temperature of the fireball through the nucleon resonances. However, later detailed theoretical investigations revealed that pions might not be so sensitive to the EoS [15, 16]. Nevertheless the pion production in heavy ion collisions has attracted continuous attention because it is the most important inelastic channel in nuclear collisions [17, 18]. The description of this process is necessary to understand the whole dynamic evolution of the fireball from the early stage to the freeze-out.

In this paper we present results on the pion production in Ru + Ru collisions at $400A$ and $1528A$ MeV. In the analysis we want to test in particular the modification of the Δ-spectral function in heavy ion collisions [19, 20] and the Coulomb interaction [21] within

*Electronic address: bhong@korea.ac.kr

the framework of the thermal model. Previously, similar ideas have been applied to the pion spectra in Au + Au collisions at $1A$ GeV by the KaoS collaboration at SIS/GSI [19, 20, 21, 22] and at $10.8A$ GeV by the E877 collaboration at AGS/BNL [23]. The experimental data are also compared to microscopic transport model calculations, namely the Isospin Quantum Molecular Dynamics (IQMD) [24, 25, 26]. Finding the common features in the interpretation of experimental data by using these two completely different approaches may shed some light on the process of particle production in relativistic nuclear collisions.

In Sec. II, the experimental setup and the method for the selection of collision centrality are described. The main experimental results on the pion spectra as functions of transverse momentum and rapidity are presented in Sec. III. In Secs. IV and V we compare the experimental data with the thermal model and the IQMD calculations, respectively. Finally, conclusions follow in Sec. VI.

II. EXPERIMENT

Collisions of $^{96}_{44}$Ru nuclei with a $^{96}_{44}$Ru target of 380 mg/cm^2 thickness were studied at $400A$ and $1528A$ MeV with the FOPI detector at SIS. The beam intensities were typically on the order of 3×10^4 ions/sec. A similar amount of events for 'central' and 'medium central' conditions was accumulated (some under 'minimum bias' conditions). The central trigger required a high multiplicity in the forward Plastic Wall (PLAWA), which covers the laboratory polar angles $\theta_{lab} = 7° - 27°$ with full azimuthal symmetry, corresponding to about 15 % of the total geometric cross section σ_{geom}. The FOPI detector system is described in detail elsewhere [27, 28].

For the tracking of charged particles we use the central drift chamber (CDC) which is placed inside a uniform solenoidal magnetic field of 0.6 T. The CDC covers $\theta_{lab} = 32° - 140°$. Pions, protons, deuterons and heavier particles are identified by using the correlation of the specific energy loss (dE/dx) and the magnetic rigidity (the laboratory momentum p divided by charge) determined by the curvature of the tracks. Details of the detector resolution and performance can be found in Refs. [27, 28, 29, 30].

To illustrate the measured phase space we show the CDC acceptance of charged pions at both beam energies in Fig. 1. In this figure, $p_t^{(0)}$ represents the normalized transverse momentum calculated by $p_t/(m_\pi \beta_{cm} \gamma_{cm})$, where p_t is the transverse momentum, m_π is the pion mass, and β_{cm} and γ_{cm} are velocity and Lorentz gamma factor of the center of mass (c.m.), respectively. In addition, $y^{(0)}$ represents the normalized rapidity $y_{lab}/y_{cm} - 1$, where y_{lab} and y_{cm} are the pion rapidity in the laboratory frame and the c.m. rapidity of the collision system, respectively. As a result, the CDC covers more than 90 % of the full solid angle when the symmetry of the colliding system around midrapidity is utilized. For both beam en-
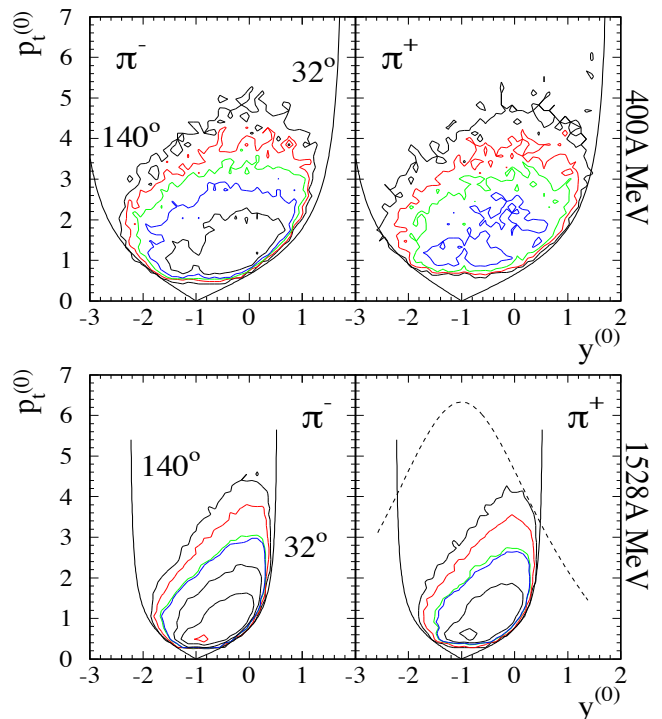

FIG. 1: Measured raw yields in the plane of normalized transverse momentum vs. normalized rapidity of π^- (left) and π^+ (right) in Ru + Ru collisions at $400A$ (top) and $1528A$ MeV (bottom). In all cases the most central 10 % of σ_{geom} have been selected. Two solid lines in each panel show the geometrical limits of the CDC. The dashed line in the lower right panel represents the upper limit of the pion laboratory momentum (800 MeV) in order to separate π^+'s from protons. Each successive contour line represents a relative factor of two in yields.

ergies a target absorption effect is visible at small p_t values near the target rapidity region ($-1.2 \leq y^{(0)} \leq -0.8$).

The collision centrality of each event is determined by two methods depending on beam energy. At $400A$ MeV the variable E_{rat} is used, defined as ratio of total transverse ($E_\perp$) to longitudinal kinetic energy ($E_\parallel$) in the center of mass:

$$E_{rat} = \sum_i E_{\perp,i} / \sum_i E_{\parallel,i}, \qquad (1)$$

where i runs over all detected charged particles in the CDC and the PLAWA. Previously, it has been demonstrated that E_{rat} is a suitable variable for event centrality, especially in central collisions at beam energies $\leq 400A$ MeV [31]. At $1528A$ MeV the total multiplicity seen in the CDC and the PLAWA is used. In this paper we select events only for the upper most 380 mb, which corresponds to $\sim$ 10 % of the total geometric cross section. Total numbers of analyzed events under these cuts are approximately 80000 at $400A$ MeV and 240000 at $1528A$ MeV. We will adopt the natural units $\hbar = c = 1$ in the following.
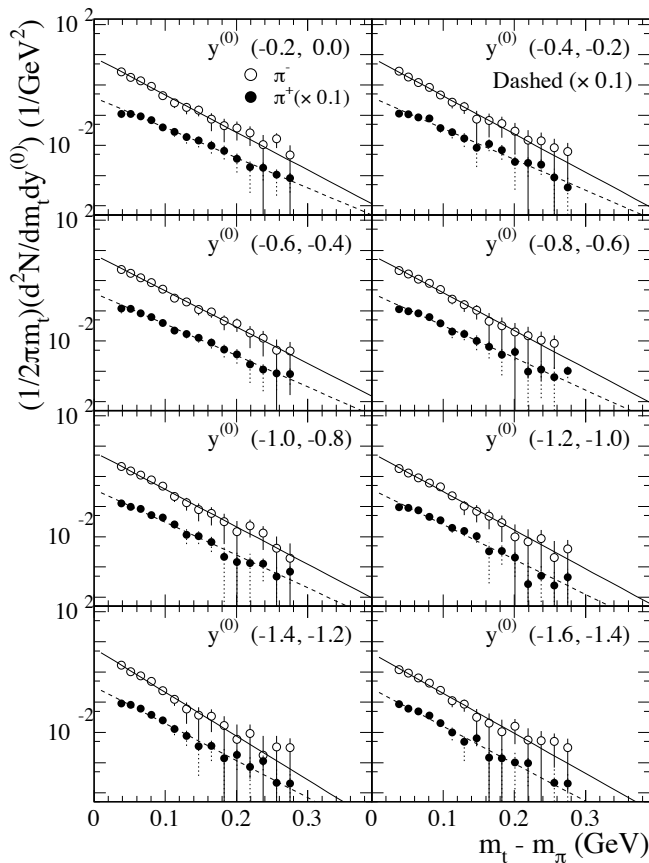
FIG. 2: Invariant spectra of π^- (open circles) and π^+ (solid circles) as a function of $m_t - m_\pi$ in Ru + Ru collisions at $400A$ MeV for the most central 10 % of σ_{geom}. The error bars represent the statistical and p_t-dependent systematic errors. Solid and dashed lines are exponential fit functions ($p_t \geq 120$ MeV) to the invariant spectra of π^- and π^+, respectively. The π^+ data and fit functions are scaled by a factor of 0.1 for a clearer display.
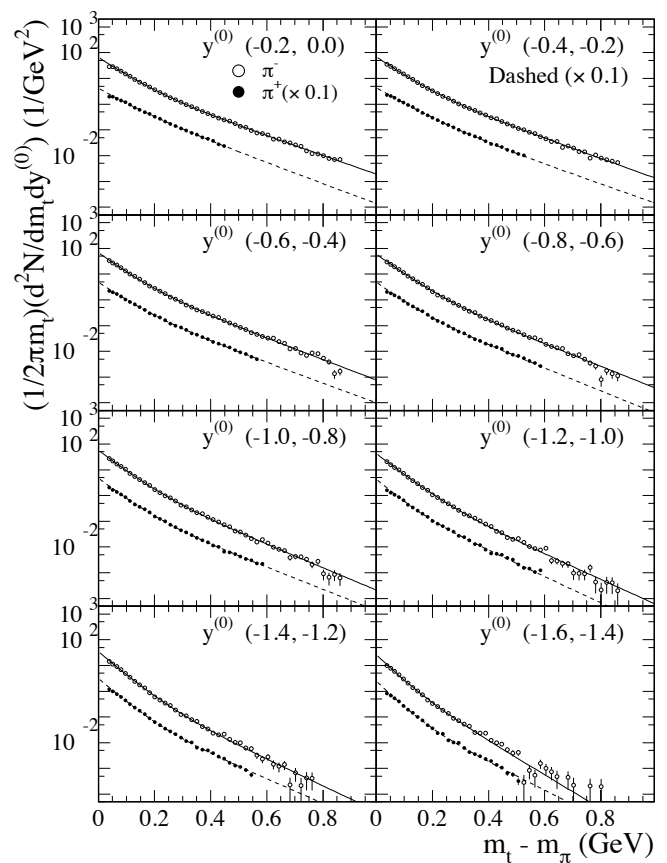
FIG. 3: Same as Fig. 2, but for $1528A$ MeV. The p_t-dependent systematic errors are negligible at this beam energy, so the error bars are dominated by statistics. Solid and dashed lines are the sum of two exponential fit functions ($p_t \geq 120$ MeV) to the invariant spectra of π^- and π^+, respectively. The π^+ data and fit functions are scaled by a factor of 0.1 for a clearer display.

III. RESULTS

Figures 2 and 3 show the experimental charged pion spectra in invariant form as a function of the transverse mass m_t ($= \sqrt{p_t^2 + m_\pi^2}$) for several rapidity bins. The spectra are corrected for the CDC track reconstruction efficiencies which are determined by a GEANT based Monte-Carlo simulation [32] taking into account the detailed response of the FOPI detector; the IQMD model was used as event generator [25]. The same method of event selection and particle identification was applied in the data analysis and in the simulation. The track reconstruction efficiencies of CDC for $\pi^\pm$ are evaluated by taking the ratio of the GEANT output to input spectra. This procedure has been applied in the two-dimensional space of p_t and $y^{(0)}$. On average these reconstruction efficiencies are determined to about 62 % and 80 % for π^+ and π^-, respectively, at $400A$ MeV. These values be-

come somewhat higher at $1528A$ MeV, namely ~ 74 % for π^+ and ~ 89 % for π^-. Note that the overall tracking efficiency depends on various parameters such as the rapidity, p_t and the track density. In general, the tracking efficiency for the algorithm used in this analysis is worse for smaller momentum. Figures 2 and 3 show the efficiency corrected spectra. More detailed discussions of the systematic errors on the invariant and the rapidity spectra will be given later in this section.

The invariant spectra of pions at $400A$ MeV exhibit a one-slope structure in all rapidity bins (Fig. 2) whereas clearly two slopes are present at $1528A$ MeV (Fig. 3). Consequently, at $400A$ MeV, the invariant spectra for each rapidity slice are fitted by one exponential function as follows:

$$\frac{1}{2\pi m_t}\frac{d^2N}{dm_t dy^{(0)}} = C(y^{(0)}) \cdot \exp[-\frac{(m_t - m_\pi)}{T_0(y^{(0)})}], \qquad (2)$$

where C and T_0 are the rapidity dependent normalization constant and the inverse slope parameter, respectively.

TABLE I: Inverse slope parameter T_0 and the measured and the extrapolated numbers of $\pi^{\pm}$ per event at midrapidity ($-0.2 < y^{(0)} \leq 0.0$) for the most central 10 % of σ_{geom}. The statistical errors are negligible whereas the estimated systematic errors are 18 and 12 % at $400A$ and $1528A$ MeV, respectively. For the later comparison, the p_t-integrated results in the same rapidity interval from the IQMD calculations are also included. For IQMD, HM and SM represent a hard and a soft EoS, respectively, including the momentum dependence of the nucleon interaction.

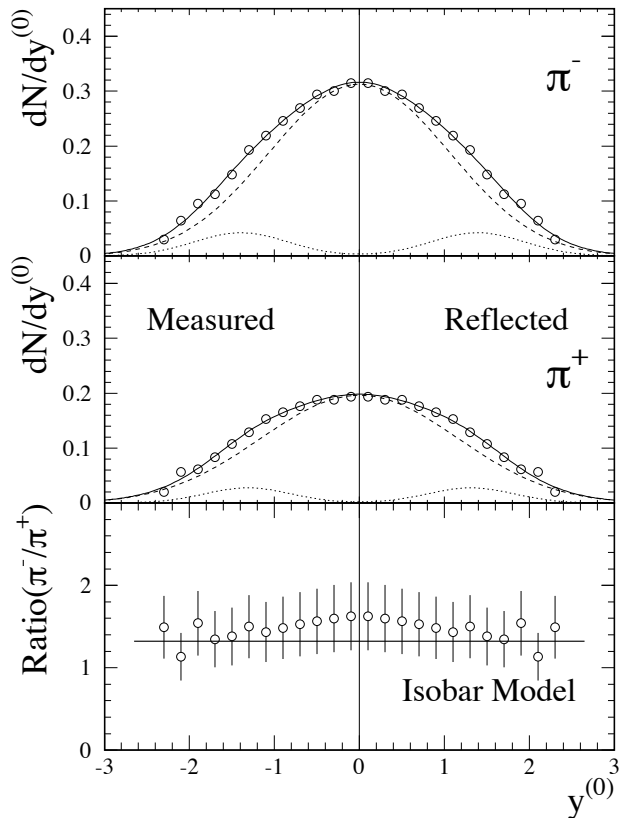|		T_0 (MeV)	Measured data ($p_t \geq 120$ MeV)	Extrapolated data	IQMD(HM)	IQMD(SM)
$400A$ MeV	π^-	35	0.11	0.32	0.46	0.45
	π^+	44	0.09	0.20	0.31	0.31
$1528A$ MeV	π^-	57 (low)/113 (high)	3.81	5.92	7.04	7.70
	π^+	62 (low)/107 (high)	3.11	4.50	5.63	6.18

FIG. 4: Rapidity distributions of π^- (top) and π^+ (middle) in Ru + Ru collisions at $400A$ MeV for the most central 10 % of σ_{geom}. Dashed and dotted lines in the two upper panels are the calculations for an isotropic thermal source at the center of mass and the estimated target/projectile components, respectively. Solid lines represent the sums of two contributions. The bottom panel shows the ratio of the rapidity distributions of π^- and π^+. The error bars in this panel consider both statistical and systematic errors, but the dominant contribution is given by the systematic errors, however. The solid horizontal line at 1.32 represents the estimated ratio of the isobar model.
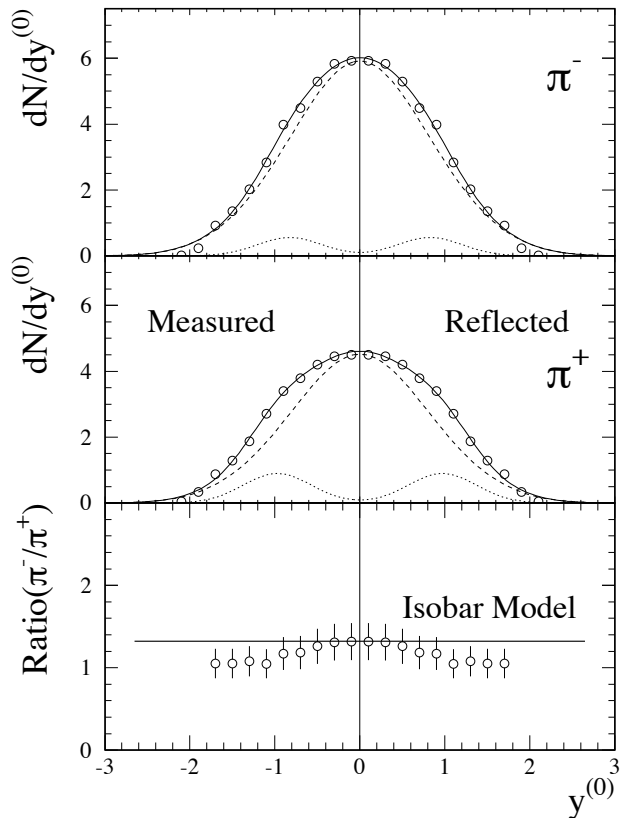
FIG. 5: Same as Fig. 4, but for $1528A$ MeV.

At $1528A$ MeV, a sum of two exponential functions is required to describe spectra. Solid and dashed lines in Figs. 2 and 3 represent the corresponding fit functions to the π^- and π^+ invariant spectra, respectively, in the range $p_t \geq 120$ MeV. Note that the one- and two-slope fit functions are the simplest phenomenological description of the pion data. The fitted T_0 values at midrapidity are listed in Table I. Since the parametrization by Eq. (2) describes the pion spectra reasonably well over all measured $m_t - m_\pi$, they are used to extract the rapidity

distributions. In details, we integrate the fitted exponential functions from $p_t = 0$ to ∞, hence also accounting for the missing p_t region in the CDC acceptance (see Fig. 1). The extrapolation to the missing low p_t region is rather significant as shown in Table I at midrapidity.

The fully extrapolated rapidity distributions are shown in the two top panels of Fig. 4 for $400A$ MeV and Fig. 5 for $1528A$ MeV, where the forward c.m. spectra are reflected around midrapidity by using the mass symmetry of the collision system. The dashed lines in Figs. 4 and 5 are the simplest thermal model predictions for an isotropic thermal source at the c.m. [33]:

$$\frac{dN_{th}}{dy^{(0)}} \propto T^3 \left(\frac{m_\pi^2}{T^2} + \frac{m_\pi}{T} \frac{2}{\cosh y_C} + \frac{2}{\cosh^2 y_C} \right) \times \exp\left(\frac{-m_\pi \cosh y_C}{T} \right), \tag{3}$$

with $y_C = y_{lab} - y_{cm}$ and $T = T_0$ at midrapidity (higher T_0 component at $1528A$ MeV). Here, T is 35 (44) MeV at $400A$ MeV and 113 (107) MeV at $1528A$ MeV for π^- (π^+). In Figs. 4 and 5 the rapidity distributions from the isotropic thermal source are normalized at midrapidity. Obviously, for both beam energies the experimental rapidity distributions of $\pi^\pm$ are wider than the isotropic thermal source sitting at midrapidity. Also represented by dotted lines are the estimated target/projectile components which are merely Gaussian fits to the differences between data and the dashed lines. The sums of the two contributions are shown by solid lines in Figs. 4 and 5.

Our strategy to integrate the exponential fits of the invariant spectra for the final $dN/dy^{(0)}$ distributions has been justified by the GEANT based Monte-Carlo simulation [32]; the input rapidity spectra agree nicely with the p_t-integrated $dN/dy^{(0)}$ distributions obtained by the exponential fits to the efficiency corrected GEANT output invariant spectra. Nevertheless the most significant source of systematic errors for the $dN/dy^{(0)}$ distribution is the uncertainty in the estimation of the CDC efficiency which relies on the tracking strategy. Such a systematic error is significant at $400A$ MeV, but it becomes much smaller at $1528A$ MeV, however. Furthermore, this uncertainty depends on p_t. It is negligible in the low p_t region (< 200 MeV), but increases with transverse momentum, reaching about 50 % at $p_t = 300$ MeV in case of the $400A$ MeV beam energy (the error bars in Figs. 2 and 3 reflect the systematic as well as statistical errors). As a result, the systematic error in the p_t-integrated $dN/dy^{(0)}$ distributions which is caused by the uncertainty of the CDC track reconstruction is estimated to about 15 % at $400A$ MeV and 6 % at $1528A$ MeV. Other sources of systematic errors which are similar at both beam energies can be summarized as follows. The systematic error in the particle identification (2 %) is determined by changing various selection criteria for good event and track samples. In addition, different fitting ranges in p_t also cause maximal 2 % uncertainty in $dN/dy^{(0)}$. The error due to the extrapolation procedure over the complete p_t-range is estimated to be about 10 %. For this estimation,

we first use various fit functions, e.g., an exponential fit in the invariant and the Boltzmann representations. Furthermore, we also use the IQMD model; the difference between the extrapolated yields by the fit functions to the data and the pion yields by IQMD for $p_t < 120$ MeV are less than 2 % at both beam energies (note that, for this test, the IQMD spectra should be normalized to the measured pion spectra for $p_t > 120$ MeV because the absolute yields by IQMD are always larger than the data as will be clear in Sec. V). Employing the IQMD model for the extrapolation to lower p_t can be supported by confirming that the yield ratios of π^- to π^+ by IQMD (independent of the EoS) agree with the estimations by the fit function to the data within 5 % for $p_t < 120$ MeV at both beam energies. Finally, assuming that the sources of various systematic errors are incoherent, we calculate overall systematic errors for the $dN/dy^{(0)}$ of both charged pions of 18 % and 12 % at $400A$ and $1528A$ MeV, respectively, by taking a quadratic sum of all contributions. Only the statistical errors are shown for the spectra presented in this paper, unless explicitly noted differently.

The pion multiplicities per event at $400A$ MeV are $< n_{\pi^-} > = 0.92 \pm 0.17(sys)$ and $< n_{\pi^+} > = 0.61 \pm 0.11(sys)$ for the most central 10 % of σ_{geom}. The resulting $< n_{\pi^-} > / < n_{\pi^+} > = 1.51 \pm 0.39(sys)$ agrees with the isobar model calculation [1], which is shown by the solid line in the bottom panel of Fig. 4, within the quoted errors. Similarly, the pion multiplicities per event at $1528A$ MeV are $< n_{\pi^-} > = 13.2 \pm 1.6(sys)$, $< n_{\pi^+} > = 11.0 \pm 1.3(sys)$, yielding $< n_{\pi^-} > / < n_{\pi^+} > = 1.2 \pm 0.2(sys)$, shown in the bottom panel of Fig. 5, again in nice agreement with the isobar model result.

IV. THERMAL MODEL

In Sec. III, we have seen the indication that the rapidity distributions of pions in central Ru + Ru collisions are wider than the isotropic thermal source at midrapidity by comparing the data with the simplest thermal model formula, Eq. (3) [33]. In order to investigate this observation further, a more instructive (but more complicated) thermal model is formulated in this section, including the decay of $\Delta(1232)$-resonances to pions explicitly.

The thermal model adopted in this paper has been described previously in Refs. [19, 20, 22, 34]. Decay pions from $\Delta(1232)$-resonances, π_Δ, and additional thermal pions, π_T, are main ingredients in this model. For the momentum spectra of $\Delta(1232)$ and π_T at freeze-out, we assume an isotropic expanding thermal source at the c.m. with the freeze-out temperature $T_f = 30$ [31] and 84 MeV [29] at $400A$ and $1528A$ MeV, respectively. Furthermore, the radial flow velocity $\beta_f = 0.3$ is included for both beam energies. We use the following expression, which was proposed by Siemens and Rasmussen for the first time in late 70's [35], for the thermal distributions
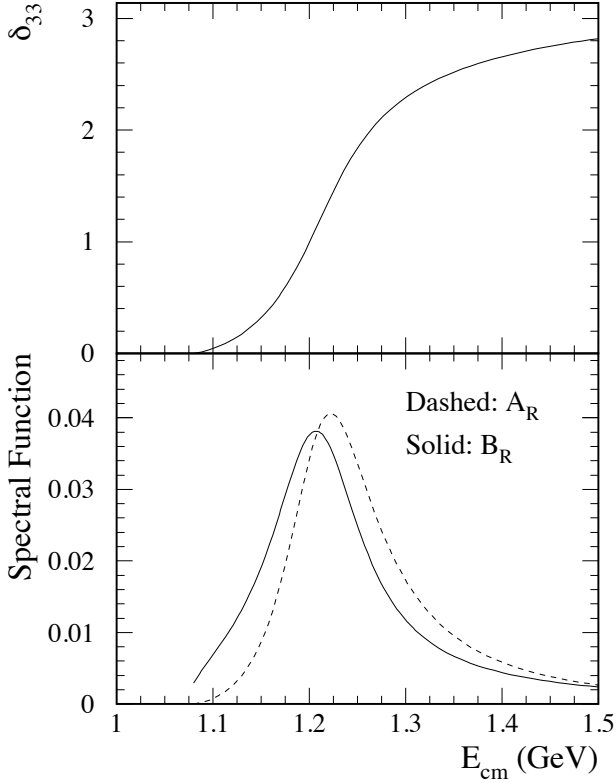
FIG. 6: Phase shift δ_{33} (top) and spectral functions of the $\Delta(1232)$-resonance (bottom). In the bottom panel, the dashed line represents a normal Breit-Wigner type function whereas the solid line represents the thermodynamic spectral function including contributions by the πN interaction [20].

of $\Delta(1232)$'s and π_T's:

$$\frac{1}{2\pi m_t}\frac{d^2 N}{dm_t dy^{(0)}} \propto E \cdot \exp\left(-\frac{\gamma E}{T_f}\right)$$
$$\times [(\gamma + \frac{T_f}{E})\frac{\sinh\alpha}{\alpha} - \frac{T_f}{E}\cosh\alpha], \quad (4)$$

where $\gamma = 1/\sqrt{1-\beta_f^2}$ and $\alpha = (\gamma \cdot \beta_f \cdot p)/T_f$. Here $E = m_t \cosh y_C$ and $p = \sqrt{p_t^2 + m_t^2 \sinh^2 y_C}$ are the total energy and respective momentum of particle in c.m.

Two different mass distributions of the $\Delta(1232)$ resonance have been considered with and without including the πN interactions in the thermal fireball. Weinhold and collaborators have exploited the detailed calculation for the thermodynamic potential of a system consisting of pions and nucleons [19, 20]. Two $\Delta(1232)$-spectral functions are shown in the bottom panel of Fig. 6, where the dashed and solid lines are for the free and the modified spectral functions, respectively. The free spectral function A_R is simply a normal Breit-Wigner shape

$$A_R(E_{cm}) = \frac{\Gamma(E_{cm})}{(E_{cm} - E_R)^2 + \Gamma(E_{cm})^2/4}, \quad (5)$$

where $\Gamma(E_{cm})$ is the energy-dependent width of the $\Delta(1232)$ [36]:

$$\Gamma(E_{cm}) = \Gamma^0 \left(\frac{k_0}{k_R}\right)^3 \frac{E_R}{E_{cm}} \left(\frac{k_R^2 + \delta^2}{k_0^2 + \delta^2}\right)^2, \quad (6)$$

where

$$E_{cm} = \sqrt{k_0^2 + m_N^2} + \sqrt{k_0^2 + m_\pi^2} \quad (7)$$

and

$$E_R = \sqrt{k_R^2 + m_N^2} + \sqrt{k_R^2 + m_\pi^2} \quad (8)$$

with m_N being the nucleon mass. The parameters used in this analysis are $\Gamma^0 = 120$ MeV, $E_R = 1232$ MeV, and $\delta = 300$ MeV, following Ref. [20].

Now considering the πN interactions, the spectral function is expected to be modified as

$$B_R(E_{cm}) = 2\frac{\partial \delta_{33}(E_{cm})}{\partial E_{cm}}, \quad (9)$$

where the phase shift of the $\Delta(1232)$-resonance (P_{33}-channel), δ_{33}, can be deduced by

$$\tan\delta_{33}(E_{cm}) = -\frac{\Gamma(E_{cm})/2}{E_{cm} - E_R}. \quad (10)$$

The phase shift factor δ_{33} is displayed in the upper panel, and the resulting $\Delta(1232)$-spectral function in the bottom panel of Fig. 6. It demonstrates a clear difference between the two spectral functions A_R and B_R, especially close to the threshold; the modified function B_R is shifted to lower masses. Note that B_R can be uniquely determined by the measured phase shift δ_{33} from Eq. (9) in a model-independent way.

In the present thermal model, the $\Delta(1232)$-resonances in the thermally equilibrated system start to decay at the surface of the fireball at freeze-out. The resulting invariant spectra of $\pi^\pm$ near c.m. (now as a function of p_t) from the thermal model calculations are shown in the left panels of Fig. 7, where the dashed lines are obtained by A_R and the solid lines are obtained by B_R. In the model calculations, thermal weighting factors are properly taken into account for both spectral functions.

In Fig. 7, the ratios of pions from the $\Delta(1232)$-decay to all pions, $\pi_\Delta/(\pi_\Delta + \pi_T)$, are determined by fitting the model calculations to the measured p_t spectra; ~ 72 % at $400A$ MeV and ~ 76 % at $1528A$ MeV. Comparing to the previous results, the estimate at $1528A$ MeV is about 12 % higher than the number estimated for smaller Ni + Ni collisions at similar beam energy ($1450A$ MeV) [34]. This implies that the fraction of projectile and target nucleons excited to $\Delta(1232)$-resonances at freeze-out is higher for a larger collision system. But this ratio does not show the beam energy dependence between $400A$ and $1528A$ MeV. One important aspect is that at $400A$ MeV the ratio $\pi_\Delta/(\pi_\Delta + \pi_T)$ is not uniquely determined with the transverse momentum spectra alone, as they
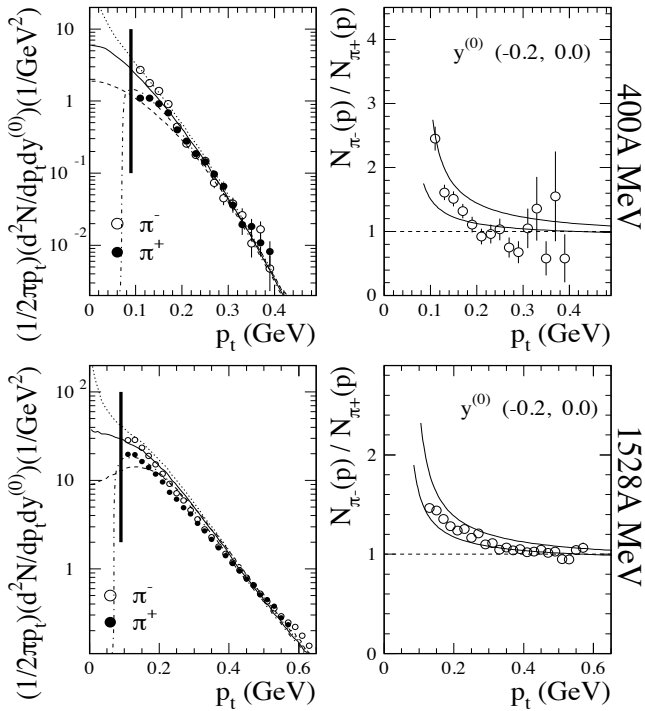
FIG. 7: (Left) Invariant spectra of $\pi^{\pm}$ at midrapidity as a function of p_t in comparison with the thermal model calculations at $400A$ (top) and $1528A$ MeV (bottom). The dashed line is obtained for the free $\Delta(1232)$-spectral function whereas the solid line is for the modified function (no Coulomb correction). The final results of the thermal model for π^- and π^+ are shown by dotted and dash-dotted lines, respectively, after the static Coulomb potential effect is taken into account. Two thick vertical solid lines represent the low-p_t limits for the validity of the present thermal model. (Right) Ratios of π^- to π^+ yields at midrapidity. Two solid lines in each panel represent the upper and lower limits utilized in the present thermal model calculation.

can be well described by one exponential function. However, by fitting the transverse momentum spectra and the yields at midrapidity simultaneously, $\pi_\Delta/(\pi_\Delta + \pi_T)$ can be uniquely fixed (see Fig. 8 and the relevant text below).

From Fig. 7 it is clear that the free spectral function A_R can not reproduce data at low p_t region ($p_t \leq 250$ MeV), and that the modified spectral function B_R can enhance the yields at low p_t, which brings the model calculation closer to the measurement. The same effect has also been observed before at similar beam energies between $1A$ and $2A$ GeV [19, 20, 22, 37].

The contributions by higher baryonic resonances, e.g., $N^*(1440)$, are negligible because of relatively low freeze-out temperature. Even in $1.9A$ GeV Ni + Ni collisions the total contribution by higher mass resonances to total pion yield has been estimated to only ~ 5 % [34], hence this factor is neglected in the present thermal model analysis for the pion yields. Besides the yield estimation,

higher mass resonances can not explain the differences in transverse momentum spectra between the data and the model calculations with A_R in the left panels of Fig. 7. If we increase the number of higher mass resonances to compensate the difference at low p_t by $N^* \rightarrow N + n\pi$ channels with $n \geq 2$, the pion contribution by $N^* \rightarrow N + \pi$ channels also increases accordingly because the branching ratios are fixed by the experimental data [38]. But the decay momenta of pions in $N^* \rightarrow N + \pi$ processes are usually larger than the ones in the $\Delta(1232)$-decay so that the shape of the spectra at higher p_t becomes much flatter than the data. Hence we conclude that the modification of the Δ-spectral function is required to describe the present pion spectra.

As next step, we consider the effect of the Coulomb potential in order to explain the observed difference between the π^- and π^+ spectra in the low-p_t region. With a static approximation for the Coulomb field [21, 23, 39], which neglects the time evolution of the fireball, $\pi^{\pm}$'s at freeze-out feel the effective Coulomb potential given by

$$V_C = \frac{Z_{eff} \cdot e^2}{R_f}, \tag{11}$$

where R_f is the radius of the fireball at freeze-out, Z_{eff} the effective charge contained in the fireball. Then, the total energy of the emitted pion is modified, depending on their charge, in the following way:

$$E(p) = E(p_i) \pm V_C, \tag{12}$$

where p_i is the initial pion momentum without Coulomb potential. Now the number of particles with momentum p, $N(p) = d^3N/dp^3$, can be related to $N(p_i)$ by the Jacobian:

$$N(p) = \left| \frac{\partial p_i^3}{\partial p^3} \right| N(p_i) = \frac{p_i E(p_i)}{p E(p)} N(p_i) = C^{\pm} N(p_i) \tag{13}$$

by using the identities $p\partial p = E\partial E$ and $\partial E(p) = \partial E(p_i)$, where

$$C^{\pm} = \sqrt{p^2 \mp 2E(p)V_C + V_C^2} \cdot \frac{E(p) \mp V_C}{p E(p)} \tag{14}$$

for positive (C^+) and negative (C^-) particles. In order to determine the strength of the Coulomb potential, V_C, the experimental yield ratios of π^- to π^+, i.e., $N_{\pi^-}(p)/N_{\pi^+}(p)$, at a given momentum p are fitted by

$$\frac{N_{\pi^-}(p)}{N_{\pi^+}(p)} = C_R \frac{\sqrt{p^2 + 2E(p)V_C + V_C^2}}{\sqrt{p^2 - 2E(p)V_C + V_C^2}}$$
$$\times \left(\frac{E(p) + V_C}{E(p) - V_C} \right) \frac{N_{\pi^-}(p_i)}{N_{\pi^+}(p_i)}, \tag{15}$$

where the normalization constant C_R and the Coulomb potential V_C are two free fit parameters to be determined by the data. The constant C_R is responsible for the height whereas V_C determines the slope of $N_{\pi^-}(p)/N_{\pi^+}(p)$ at low p_t. The right panels of Fig. 7 show

the comparisons of the data with thermal model calculations at both beam energies, assuming the same momentum dependence of $\pi^\pm$ spectra before the Coulomb correction, $N_{\pi^-}(p_i) = N_{\pi^+}(p_i)$ in this case. The values of $C_R = 0.9$ and $V_C = 17 \pm 6$ MeV describe data well at $400A$ MeV, especially in the low-p_t region where the $\pi^\pm$ spectra differ significantly. Similarly, $C_R = 0.9$ and $V_C = 16 \pm 4$ MeV are the best set of parameters at $1528A$ MeV. The agreement between the data and the model calculations in $N_{\pi^-}(p)/N_{\pi^+}(p)$ at midrapidity is reasonable at both beam energies. Note that the same analysis technique as in this paper can reproduce the $\pi^\pm$ spectra, measured in Au + Au collisions at $1A$ GeV by the KaoS collaboration, with $V_C = 25$ MeV [22].

It should be emphasized that the dynamical consideration becomes important only when the velocity of pions is smaller than the surface expansion velocity (β_s) of the fireball [39]. Charged pions with the velocity larger than β_s see a time-independent Coulomb potential, and the present thermal model is applicable only for those pions. For the average radial flow velocity $\beta_f = 0.3$, β_s is about 0.40 (or 0.53) by assuming a linear (or quadratic) flow profile as a function of the fireball radius. Then, the critical momentum ($m_\pi\gamma_s\beta_s$) of pion is about 60 (90) MeV for the linear (quadratic) flow profile. These estimated limits, shown by thick vertical solid lines in the left panels of Fig. 7, are close to or slightly lower than the low-p_t limit of our measured pion spectra, which is about 100 MeV.

By using the determined values of V_C, we can generate the invariant spectra of $\pi^\pm$ by Eqs. (13) and (14) at $400A$ and $1528A$ MeV. The dotted and dash-dotted lines in the left panels of Fig. 7 represent the final invariant spectra obtained by the thermal model for π^- and π^+, respectively, after the Coulomb correction is included. Good agreement between the data and the thermal model calculations can be found.

Once having estimated the magnitude of the Coulomb potential, one can deduce the source size at thermal freeze-out by using Eq. (11). The centrality condition used in this analysis corresponds to the average geometrical impact parameter $< b_{geom} >$ of ~ 2.3 fm. The evaluated number of participant nucleons (A_{part}) can be estimated to about 146 by employing the recipe given in Ref. [40]. After scaling with Z/A of projectile and target, one obtains $Z_{eff} \approx 66.7$. The corresponding freeze-out radii $R_f = Z_{eff}\cdot e^2/V_C$ are 5.6 ± 2.0 fm at $400A$ MeV and 6.0 ± 1.5 fm at $1528A$ MeV. These results demonstrate that the thermal freeze-out radius is almost independent of the beam energy. We also compare the freeze-out radii estimated in this paper with two other published values that were obtained by using the same method. Having applied the present thermal model to the KaoS spectra at the SIS, the pion freeze-out radius was estimated as 6.3 ± 0.5 fm for Au + Au collisions at $1A$ GeV [22]. When the same model was applied to the E877 spectra at the AGS, the pion freeze-out radius was estimated as 6.4 ± 4.5 fm for Au + Au collisions at $10.8A$ GeV [23].

TABLE II: Comparison of the ratio of the estimated pion freeze-out radius R_f to the sharp-sphere radius R_0 ($= 1.2A^{1/3}$ fm) of the projectile (or target) nucleus at different beam energies (E_b).

E_b (A GeV)	System	Centrality (%)	R_f/R_0
0.4	Ru + Ru	10	1.0 ± 0.4
1.0	Au + Au	14	0.9 ± 0.2
1.5	Ru + Ru	10	1.1 ± 0.3
10.8	Au + Au	4	0.9 ± 0.6

Although the error in the AGS result is too big to draw any meaningful conclusion, the mean radii do not show any beam energy dependence for Au + Au collisions, too. It is not possible to compare directly the present results with other numbers mentioned above because the system size is not the same (the mass number of Au is more than twice that of Ru). Therefore, we compare the ratio of the estimated freeze-out radius R_f to the radius of the projectile (or target) nucleus. The results are summarized in Table II; the resulting ratios are very similar at different beam energies between $0.4A$ and $10.8A$ GeV despite of a small difference in the collision centrality.

Only the midrapidity p_t spectra of pions are tested for the present thermal model . At forward and backward rapidities, the situation is more complicated because of the observed incomplete stopping and partial transparency of projectile and target nuclei at these beam energies [29, 41, 42, 43]. Figure 8 shows the measured rapidity spectra of $\pi^\pm$'s in comparison with the thermal model calculations; the data and the model calculations are compared only for $p_t \geq 120$ MeV due to the uncertainty of the spectral shape at the low-p_t region in the present thermal model, which are indicated by thick vertical solid lines in Fig. 7. This comparison demonstrates that the thermal model calculations, assuming isotropic midrapidity thermal source, give somewhat narrower rapidity distributions than the data at both beam energies. In order to reproduce the full measured rapidity spectra, the longitudinally elongated, rather than isotropic, thermal source of $\Delta(1232)$-resonances and pions should be assumed. Although this kind of adjustment is, in principle, possible by changing the widths of the rapidity distributions of $\Delta(1232)$'s and π_T's, we do not attempt to calculate the exact rapidity spectra of pions at present.

V. COMPARISON WITH IQMD

The Isospin Quantum Molecular Dynamics (IQMD) model is a nonequilibrium transport model which considers the isospin degree of freedom for the nucleon-nucleon cross section and the Coulomb interaction [25]. In the framework of the IQMD model, pions are explicitly formed via the decay of the Δ-resonances, and experimental cross sections are considered. The IQMD version
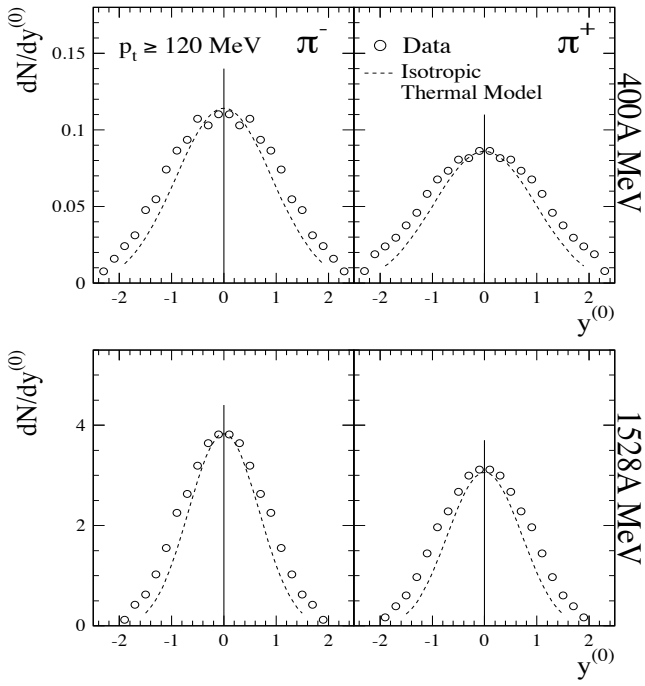
FIG. 8: Measured rapidity spectra of π^- (left) and π^+ (right) in comparison with the thermal model calculations at $400A$ (top) and $1528A$ MeV (bottom). The results from the thermal model, shown by the dashed lines, are obtained with isotropic thermal source at midrapidity. The modified $\Delta(1232)$-spectral function and Coulomb correction are included. Due to the low-p_t limit of applicability for the present thermal model (thick vertical solid lines in Fig. 7), the data and the model calculations are compared only for $p_t \geq 120$ MeV.

utilized in this analysis contains only the lowest three Δ-states. A modified detailed balance treatment, which accounts for their finite width, is also considered. As a consequence, the appearing spectral shape of Δ's is changing in the course of the reaction. Therefore, in the charged pion spectra, the IQMD model has to show, in principle, the effects of the Coulomb interaction in addition to other collision effects including the πN interactions.

IQMD has been successful in reproducing various aspects of heavy ion collisions, including the pion production in Au + Au collisions at $1A$ GeV [26]. In this section, we compare the present experimental pion spectra with the IQMD calculations in Ru + Ru collisions at $400A$ and $1528A$ MeV. For these calculations, a hard (compressibility $K = 380$ MeV) and a soft ($K = 200$ MeV) EoS versions are used, including the momentum dependence of the nucleon interaction (MDI); they are denoted by IQMD(HM) and respective IQMD(SM) in the following. Note that the IQMD events are analyzed with the same analysis procedure as the data. As in the data analysis, we also use the E_{rat} distribution at $400A$ MeV to select the most central 10 % of σ_{geom} whereas at $1528A$ MeV the total multiplicity measured in the PLAWA and
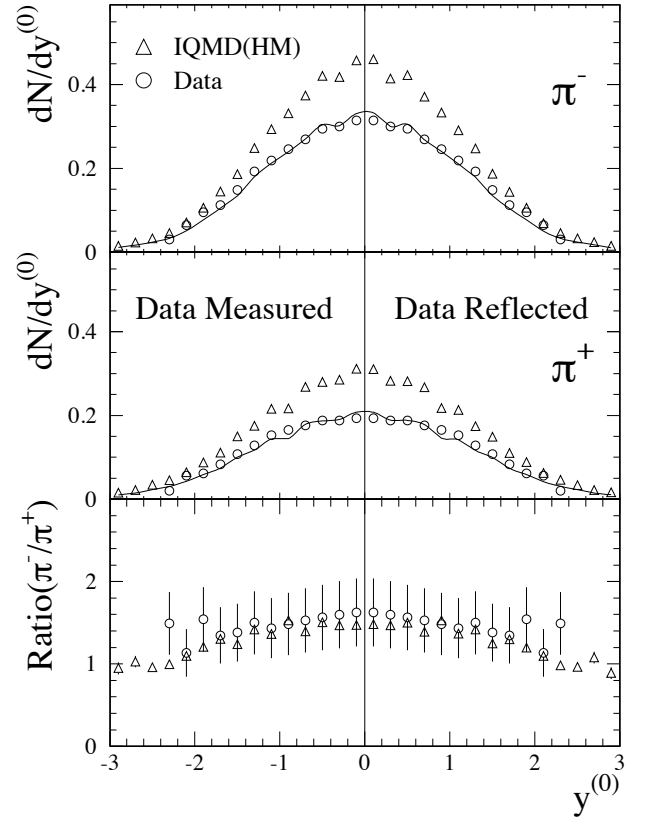

FIG. 9: Comparison of data (circles) with the IQMD(HM) calculations (triangles) for the rapidity distributions of π^- (top) and π^+ (middle) in Ru + Ru collisions for the most central 10 % of σ_{geom}. Solid lines in these two panels show the IQMD(HM) calculations normalized to the total experimental yields of $\pi^\pm$. The bottom panel shows the ratio of the π^- and π^+ distributions, both for data and model results. Results from IQMD(SM) are almost identical to those from IQMD(HM) so that we omit in these plots.

the CDC acceptance is taken.

Top and middle panels of Figs. 9 and 10 show the comparisons of the experimental $dN/dy^{(0)}$ spectra (circles) with the IQMD(HM) calculations (open triangles) for π^- and π^+, respectively. The IQMD(SM) calculations (inverted solid triangle) are almost identical with IQMD(HM) at $400A$ MeV, but they are about 10 % larger in yields for both charges at $1528A$ MeV. Therefore, we include these results only in Fig. 10 at the higher beam energy.

In accordance with earlier investigations [44], we find that the IQMD model produces too many pions in Ru + Ru collisions, especially at $400A$ MeV. In order to compare the shape of the $dN/dy^{(0)}$ spectra, we need to scale the IQMD results by 0.72 and 0.67 for π^- and π^+, respectively, at $400A$ MeV for both HM and SM (solid lines in Fig. 9). These scale factors are determined in such a way that the integration of the model $dN/dy^{(0)}$ yields
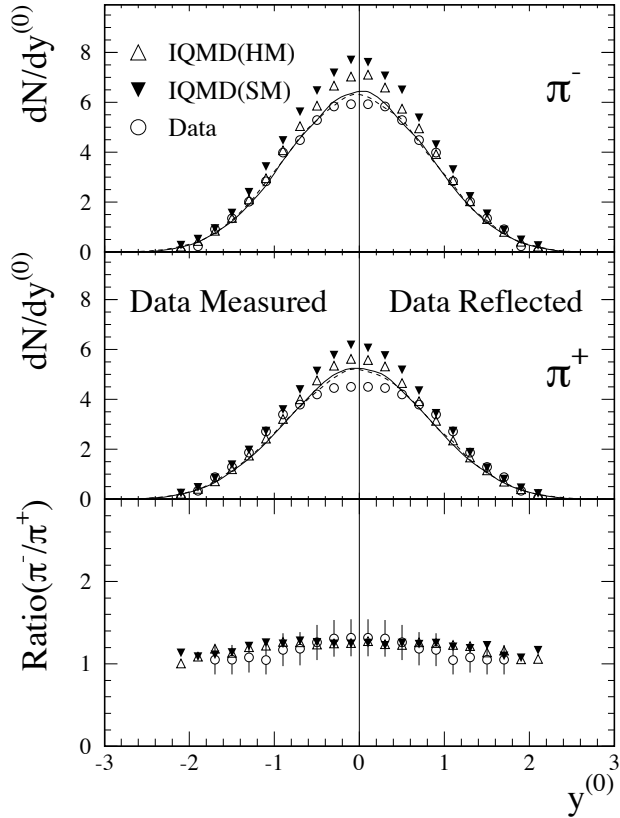
FIG. 10: Same as Fig. 9, but for $1528A$ MeV. Inversed filled triangles represent the IQMD(SM) calculation. Dashed lines in top two panels show the IQMD(SM) calculations normalized in such a way that total yields of $\pi^{\pm}$ are the same as data.

the same value as the integrated data distribution. Similarly, we also need to scale the IQMD results by 0.90 for π^- and 0.93 for π^+ at $1528A$ MeV with HM (solid lines in Fig. 10). On the other hand, this scaling factor is reduced to 0.82 for π^- and 0.84 for π^+ with the choice of SM (dashed lines in Fig. 10). The scaled $dN/dy^{(0)}$ distributions from the IQMD calculations can nicely reproduce the shape of the measured $dN/dy^{(0)}$ spectra of pions at both beam energies. The bottom panels of Figs. 9 and 10 show that the ratios of the $dN/dy^{(0)}$ distributions of π^- and π^+ agree with the data within errors at both beam energies.

The left panels of Fig. 11 display the comparisons of data with the model calculations for the invariant spectra of $\pi^{\pm}$ at midrapidity. Similar to the experimental data, the IQMD(HM) calculations show different shapes for π^- and π^+ in the low transverse momentum region, which can be attributed to the Coulomb interaction. These differences can be presented more clearly in the ratio $N_{\pi^-}(p)/N_{\pi^+}(p)$ as a function of p_t (right panels of Fig. 11). The IQMD(HM) calculation agrees very nicely with the data. The IQMD(SM) calculation gives very
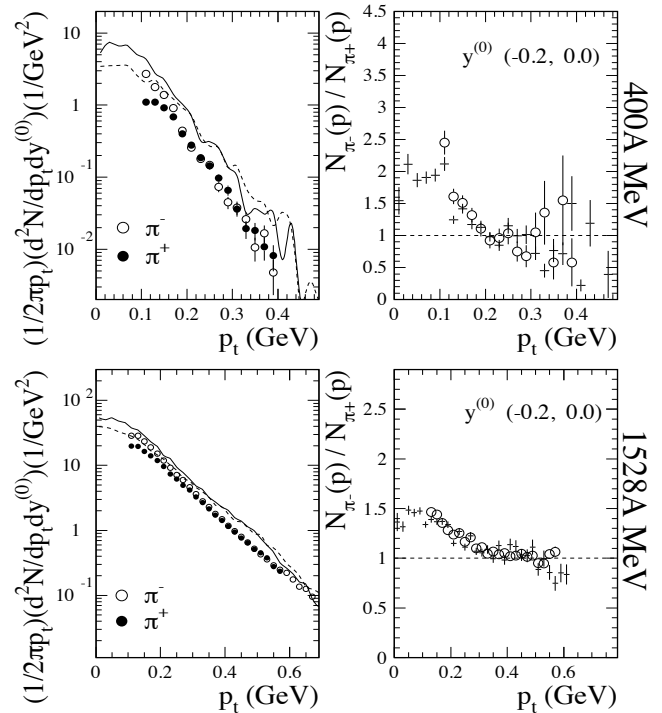

FIG. 11: (Left) Invariant spectra of $\pi^{\pm}$ at midrapidity as a function of p_t in comparison with the IQMD(HM) calculations, shown by solid and dashed lines for π^- and π^+, respectively. (Right) Ratio of π^- to π^+ yields at midrapidity. Crosses are from the IQMD(HM) calculations. Results from the IQMD(SM) are very similar to those from the IQMD(HM) except about 10 % higher yield at $1528A$ MeV. Top and bottom panels are for the data and the model calculations at $400A$ and $1528A$ MeV, respectively.

similar results on the transverse momentum spectra of pions and their ratios except about 10 % higher production than HM at $1528A$ MeV.

VI. CONCLUSIONS

We have presented charged pion spectra in central Ru + Ru collisions at $400A$ and $1528A$ MeV. In both beam energies the uppermost 10 % of the geometric cross section have been selected. The measured transverse momentum spectra in their invariant form as a function of m_t can be described very well by one exponential function at $400A$ MeV and by a sum of two exponential functions at $1528A$ MeV.

The results from thermal model have been compared to the transverse momentum spectra of pions at midrapidity. Pions from the decay of the thermal $\Delta(1232)$-resonances in addition to thermal pions are main ingredients of the present thermal model. The momentum distributions of $\Delta(1232)$-resonances and thermal pions at freeze-out are assumed to be an expanding isotropic source at the center of mass. Pion spectra at low

transverse momentum require the modification of the $\Delta(1232)$-spectral function due to the πN interactions at both beam energies. The Coulomb potential is necessary to explain the different spectral shapes between the π^- and π^+ spectra in the low transverse momentum region. With this we find excellent agreement between the data and the thermal model calculations. Using the estimated strength of the Coulomb potential, which is determined by the momentum dependent yield ratio of π^- to π^+, the freeze-out radius of the fireball has been deduced to be about 6.0 fm at both $400A$ and $1528A$ MeV. The rapidity spectra of pions require the longitudinally elongated (not isotropic) thermal source of Δ's and pions.

Finally, the experimental data are compared to IQMD model calculations. Although the absolute yields of charged pions in the model are somewhat larger (about 30 and 10 % at $400A$ and $1528A$ MeV, respectively), the shapes of the rapidity and transverse momentum spectra agree nicely with the data. The IQMD model displays that the yield ratios of π^- to π^+ at low transverse momenta deviate from unity due to the Coulomb interaction; the agreement between the data and the IQMD model is satisfactory. The pion yield is independent of the choice of the equation of state at $400A$ MeV, whereas it is about 10 % higher with a soft than with a hard EoS at $1528A$ MeV . The comparison of the pion transverse momentum and rapidity spectra with two completely different approaches (thermal model and IQMD) renders us the importance of the Coulomb interaction and the collision effects including the πN interactions in the pion spectra at SIS energies.

[1] R. Stock, Phys. Rep. **135**, 259 (1986).
[2] H. Stöcker and W. Greiner, Phys. Rep. **137**, 277 (1986).
[3] G. E. Brown, Phys. Rep. **163**, 167 (1988).
[4] A. Sandoval, R. Stock, H. E. Stelzer, R. E. Renfordt, J. W. Harris, J. P. Brannigian, J. V. Geaga, L. J. Rosenberg, L. S. Schroeder, and K. L. Wolf, Phys. Rev. Lett. **45**, 874 (1980).
[5] S. Nagamiya, M. C. Lemaire, E. Moeller, S. Schnetzer, G. Shapiro, H. Steiner, and I. Tanihata, Phys. Rev. C **24**, 971 (1981).
[6] KaoS Collaboration, D. Brill *et al.*, Phys. Rev. Lett. **71**, 336 (1993).
[7] TAPS Collaboration, O. Schwalb *et al.*, Phys. Lett. B **321**, 20 (1994).
[8] FOPI Collaboration, D. Pelte *et al.*, Z. Phys. A **357**, 215 (1997).
[9] FOPI Collaboration, D. Pelte *et al.*, Z. Phys. A **359**, 55 (1997).
[10] B. Hong for the FOPI Collaboration, J. Korean Phys. Soc. **43**, S32 (2003).
[11] W. Reisdorf and H. G. Ritter, Annu. Rev. Nucl. Part. Sci. **47**, 663 (1997).
[12] J.-Y. Ollitrault, Nucl. Phys. **A638**, 195c (1998).
[13] P. Senger and H. Ströbele, J. Phys. G **25**, R59 (1999).
[14] H. Stöcker, A. A. Ogloblin, and W. Greiner, Z. Phys. A **303**, 259 (1981).
[15] G. F. Bertsch, H. Kruse, and S. Das Gupta, Phys. Rev. C **29** R673 (1984).
[16] H. Kruze, B. V. Jacak, and H. Stöcker, Phys. Rev. Lett. **54**, 289 (1985).
[17] DIOGENE Collaboration, J. Poitou *et al.*, Nucl. Phys. **A536**, 767 (1992).
[18] E895 Collaboration, J. L. Klay *et al.*, Phys. Rev. C **68**, 054905 (2003).
[19] W. Weinhold, B. Friman, and W. Nörenberg, Phys. Lett. B **433**, 236 (1998).
[20] W. Weinhold, Ph. D. Thesis, Technische Universität Darmstadt, Germany, 1998.
[21] KaoS Collaboration, A. Wagner *et al.*, Phys. Lett. B **420**, 20 (1998).
[22] B. Hong, J. Korean Phys. Soc. **38**, L291 (2001).
[23] E877 Collaboration, J. Barrette *et al.*, Phys. Rev. C **62**, 024901 (2000).
[24] J. Aichelin, Phys. Rep. **202**, 233 (1991).
[25] C. Hartnack, Rajeev K. Puri, J. Aichelin, J. Konopka, S. A. Bass, H. Stöcker, and W. Greiner, Eur. Phys. J. A **1**, 151 (1998).
[26] S. A. Bass, C. Hartnack, H. Stöcker, and W. Greiner, Phys. Rev. C **51**, 3343 (1995).
[27] FOPI Collaboration, A. Gobbi *et al.*, Nucl. Instrum. and Methods A **324**, 156 (1993).
[28] J. Ritman for the FOPI Collaboration, Nucl. Phys. (Proc. Suppl.) **B44**, 708 (1995).
[29] FOPI Collaboration, B. Hong *et al.*, Phys. Rev. C **57**, 244 (1998).
[30] FOPI Collaboration, D. Best *et al.*, Nucl. Phys. **A625**, 307 (1997).
[31] FOPI Collaboration, W. Reisdorf *et al.*, Nucl. Phys. **A612**, 493 (1997).
[32] GEANT-Detector Description and Simulation Tool, CERN Program Library Long Writeup W5013 (CN Division, CERN, 1993).
[33] E. Schnedermann, J. Sollfrank, and U. Heinz, Phys. Rev. C **48**, 2462 (1993).
[34] FOPI Collaboration, B. Hong *et al.*, Phys. Lett. **B407**, 115 (1997).
[35] P. J. Siemens and J. O. Rasmussen, Phys. Rev. Lett. **42**, 880 (1979).
[36] J. H. Koch, N. Ohtsuka, and E. J. Moniz, Ann. Phys. (NY) **74**, 99 (1984).
[37] FOPI Collaboration, M. Eskef *et al.*, Eur. Phys. J. A **3**, 335 (1998).
[38] Particle Data Group, C. Caso *et al.*, Eur. Phys. J. C **3**, 1 (1998).
[39] A. Ayala and J. Kapusta, Phys. Rev. C **56**, 407 (1997).
[40] J. Gosset, H. H. Gutbrod, W. G. Meyer, A. M. Poskanzer,

A. Sandoval, R. Stock, and G. D. Westfall, Phys. Rev. C **16**, 629 (1977).

[41] FOPI Collaboration, B. Hong *et al.*, Phys. Rev. C **66**, 034901 (2002).

[42] B. Hong for the FOPI Collaboration, Nucl. Phys. **A721**, 317c (2003).

[43] FOPI Collaboration, W. Reisdorf *et al.*, Phys. Rev. Lett. **92**, 232301 (2004).

[44] M. R. Stockmeier, W. Reisdorf, N. Herrmann, M. Merschmeyer, D. Pelte, and K. Wisniewski, *GSI Scientific Report 2001-1* (GSI, Germany, 2002) p. 35.